3D PIC simulations of collisionless shocks at lunar magnetic anomalies and their role in forming lunar swirls

R.A. Bamford, E.P. Alves, F. Cruz, B. J. Kellett, R. A. Fonseca, L.O Silva, R.M.G.M. Trines, J.S. Halekas, G. Kramer, E. Harnett, R.A. Cairns and R. Bingham

Published version information

Citation: RA Bamford et al. '3D PIC simulations of collisionless shocks at lunar magnetic anomalies and their role in forming lunar swirls.' Astrophys J, vol. 830, no. 2 (2016): 146.

DOI: 10.3847/0004-637X/830/2/146

3D PIC simulations of collisionless shocks at lunar magnetic anomalies and their role in forming lunar swirls

R.A. Bamford,[1,*] E.P. Alves,[2] F. Cruz,[2] B. J. Kellett,[1] R. A. Fonseca,[3] L.O Silva,[2]
R.M.G.M. Trines,[4] J.S. Halekas,[5] G. Kramer,[6] E. Harnett,[7] R.A. Cairns,[8] and R. Bingham[9,†]

[1] *RAL Space, STFC, Rutherford Appleton Laboratory, Chilton, Didcot, OX11 0QX, UK.*
[2] *GoLP/Instituto de Plasmas e Fusão Nuclear, Instituto Superior Técnico, Universidade de Lisboa, 1049-001 Lisbon, Portugal*
[3] *DCTI/ISCTE - Instituto Universitário de Lisboa, 1649-026 Lisbon, Portugal*
[4] *Central Laser Facility, STFC, Rutherford Appleton Laboratory, Chilton, Didcot, OX11 0QX, UK.*
[5] *Department of Physics and Astronomy, 414 Van Allen Hall, University of Iowa, Iowa City, IA 52242, U.S.A.*
[6] *The Lunar and Planetary Institute, USRA, 3600 Bay Area Blvd, Houston, Texas 77058, USA*
[7] *Department of Earth and Space Science, University of Washington, Seattle, WA 98195-1310, USA*
[8] *University of St Andrews, North Haugh, St. Andrews, Fife, KY16 9SS, UK.*
[9] *SUPA, University of Strathclyde, Glasgow, Scotland, 4G 0NG,U.K.*

(Dated: 18/07/2016)

ABSTRACT

Investigation of the lunar crustal magnetic anomalies offers the most comprehensive long-term data set of observations of small scale magnetic fields and their interaction with the solar wind. In this paper a review of the observations of lunar mini-magnetospheres is compared quantifiably with theoretical kinetic scale plasma physics and 3D particle-in-cell (PIC) simulations. The aim in this paper is to provide a complete picture of all aspects of the phenomena and show how the observations from all the different and international missions interrelate.

The analysis shows that the simulations are consistent with the formation of miniature (smaller than the ion Larmor orbit) collisionless shocks and miniature magnetospheric cavities. Something that has not been demonstrated previously.

The simulations reproduce the finesse and form of differential proton patterns that are believed to be responsible for the creation of both the 'lunar swirls' and 'dark lanes' [1].

By using a mature plasma physics code like OSIRIS [2], allows for the first time a side-by-side comparison between model and space observations. This is shown for all of the key plasma parameters observed by spacecraft to date, including the spectral imaging data of the lunar swirls [3]. The analysis of miniature magnetic structures allows insight into multi-scale mechanisms and kinetic scale aspects of planetary magnetospheres.

INTRODUCTION

The Moon does not have an active core dynamo with which to generate its own global magnetic field [4]. It does, however, have several small, static regions of low magnetic field ($\sim 50 - 500\ nT$) on the surface [5, 6]. The distribution of these magnetic field anomalies on the Moon, varies from 1000s of kilometres across, irregular conglomerations and clusters, to relatively small (100s of kilometres across) and isolated features - such as the Reiner Gamma formation and Gerasimovich magnetic anomaly [7–10]. The largest distributions of crustal magnetic anomalies are located on the southern part of the farside of the Moon, antipodal to the Crisium, Serenitatis, Imbrium, and Orientale basins [7–10]. The presence of small areas of magnetic field on an otherwise unmagnetised planetary body is not unique to the Moon. Mars, Mercury and some asteroids are known to also possess small scale magnetic fields [11–13].

Figure 1 shows a graphical summary of the in-situ observations from many spacecraft that intersected the mini-magnetospheres formed as a result of the solar wind interacting with the magnetic anomalies on the Moon's surface. The computational investigation into mini-magnetospheres has become an area of considerable interest. A number of papers on hybrid[14–17] and particle-in-cell[17–27] simulations have been applied following on from previous MHD simulations [28–30]. Here we do fully self-consistent particle-in-cell simulations in 2D and 3D, with realistic proton–to–electron mass ratio. This provides for the first time a direct comparison with theory and observational signatures for a small (sub-ion Larmor radius), isolated magnetic anomaly forming a collisionless shock.

We have reproduced all the major observational characteristics of lunar swirls using the simplest of magnetic topologies - a single dipole, under a variety of orientations and solar wind conditions. Low beta, magnetized solar wind flows with Alfvèn Mach numbers between 2-8 used here, are consistent with the formation of laminar and turbulent quasi-perpendicular collisionless shocks studied by numerical methods for planetary magnetospheres (e.g.[45–49]).

In this paper we review the observational data taken by all spacecraft to date. This is compared with results from a particle-in-cell code providing a one-to-one correspon-

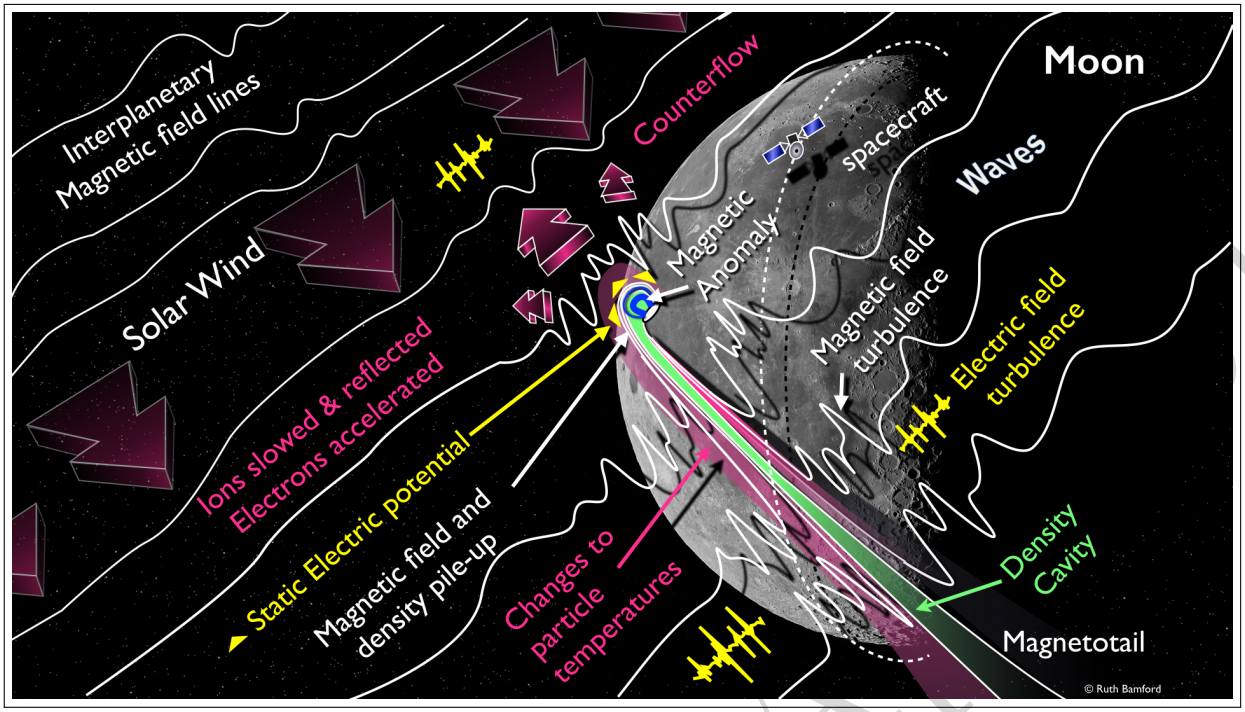

FIG. 1: A graphical summary of the spacecraft observational data [31–40] of Lunar mini-magnetospheres. The Solar Wind plasma with an embedded magnetic field, encountering the small ($\sim 10-100km$) crustal magnetic field ($\sim 400nT$) on the lunar surface, producing a "mini-magnetosphere". The mean value of the solar wind magnetosonic Mach number is $M_m = 8$ [41], with a $\beta = 0.2$. A shock-like discontinuity in density and magnetic field can occur as low as $\sim 10-20km$ above the surface [40] and with a magnetotail that is drawn out into space by 10,000s km [36]. The width of the barrier region is very narrow $\sim 1-2km$. Within the barrier plasma is less turbulent within the diamagnetic cavity and much of the incoming proton density has been excluded [33]. Upstream of the narrow interface region however, increased levels of magnetic and electrostatic turbulence, including Whistlers-modes [42, 43], are observed, with waves occurring at or near the local lower-hybrid plasma frequency and Alfvén waves [44]. The source of the turbulence and waves being counter streaming protons is reflected back by the magnetic boundary. The observations of the plasma particle distributions show a slowing and reversing of flow of the protons accompanied by a cooling upon approaching the magnetopause. Conversely the electrons experience an acceleration towards the anomaly and heating across the transition[44]. The simultaneous accelerations and deaccelerations of opposite charges implies the existence of sizeable ($\approx 100-400V/m$), static electric field pointing anti-moonward above the magnetic anomaly site [44]. The changes of temperature indicate a non-adiabatic dissipative interaction between solar wind protons and lunar magnetic anomalies.

dence. Figure 1 shows a summary of the accumulated observations.

The simulations quantifiably confirm the satellite [40] findings and the theoretical predictions [50], that a miniture collisionless shock can be responsible for all the observations[31–40]. Here it is confirmed that the interaction or boundary layer can form well (kilometers) above the lunar surface (depending upon conditions) and need not be a photoelectric sheath [51] restricted to a metres above the surface. A 2D parametric analysis of dipole characteristics illustrates how the primary driving term in generating the electric field is the gradient in energy density, therefore it is not exclusive to one magnetic field orientation or magnetic mirroring. Asymmetries appear in the diamagnetic cavity due to differences in the preferred plasma instabilities, their growth and interchange rates.The parametric analysis also shows how observational verification of the formation of the very smallest mini-magnetospheres and collisionless shocks, may be very difficult to determine due to the relative spacecraft speed and dipole size.

The analysis of mini-magnetospheres is very interesting for fundamental plasma physics. Their occurrence in space means that non-intrusive measurements are possible including particle distributions functions. The fact that they are located on our nearest planetary body also provides a high level of diverse observational data.

Particular astronomical interest in mini-magnetospheres is provided by the apparent link between the mini-magnetospheres and the 'lunar swirl'

patterns on the Moon [7, 52–54]. The analysis here shows how the fine structure observed within the swirls, as well as the narrow enhanced 'dark lanes', can be reproduced by the fine scale plasma interactions at the same approximate dimensions and magnetic field strengths.

LUNAR SWIRLS AND MAGNETIC ANOMALIES

Lunar swirls are optically distinct, white surface features that are found in several locations across the Moon's surface [55]. The features are distinctive due to their fluid or wispy structure that is unlike either craters or impact ejecta. Their form has been determined to be unrelated to geographical topography and appears to overprint on both mountainous and plateau terrain [56–58]. Although not all magnetic field anomalies have identifiable lunar swirl patterns, no lunar swirls have been found that are not co-incident with similar sized areas of anomalous crustal magnetic field [3, 58].

Several theories exist to explain the creation of lunar swirls [12, 59, 60]. Recent work [61, 62] on spectral data from the Diviner Lunar Radiometer on Lunar Reconnaissance Orbiter, Moon Mineralogy Mapper on board Chandrayaan-1 [3] and spectrometer data from Clementine [58, 63, 64], strongly supports the hypothesis that the mechanism of the variations in albedo is related to differential solar wind/magnetospheric proton bombardment of the lunar regolith.

Proton bombardment reddens (darkens) the lunar regolith over time [1]. Persistent reduced proton flux leads to a 'lighter' colour, while extra enhanced proton flux leads to an even 'darker' appearance. The interplay between the two results in 'white wisps' interspersed with narrow 'dark lanes' [3, 58, 61–63].

This spectroscopic data means that the lunar swirls are the first diagnostic observation directly linked to the interaction of the solar wind with the mini-magnetosphere above and onto the lunar surface. The interaction causes deflection of solar wind protons away from the 'on-swirl' [3] surfaces and focuses them onto 'off-swirl' [3] surfaces. The additional concentration of protons on to the narrow 'dark lanes'[58] enhances the spectral darkening effects of space weathering significantly, relative to normal lunar surfaces.

The formation and retention of the level of detail visible in the swirls requires a very precise and semi-consistent redirection of proton flux. The finesse of the transitions seen in the swirls (sometimes less than 1 kilometer) further suggests that the process close (0-10s km) to the surface is tightly held by the magnetic footprint. A large scale, remote plasma structure would be shifted and dispersed by the fluctuations in the solar wind and lunar cycle and effects of transitions in and out of the regions of the Earth's magnetosphere, these cycles are likely to be the cause of the 'wispiness' of swirls.

THE SIGNIFICANCE OF THE SCALE SIZE OF MAGNETIC ANOMALIES

The overall size of an isolated magnetic anomaly like the Gerasimovich magnetic anomaly is of the order of, or smaller than, the interplanetary plasma proton Larmor (gyro) radius r_{Li} in the interplanetary magnetic field (B_{IMF}). For example $r_{Li} \sim 500\ km$ for a 450 kms^{-1} proton in a $B = 10nT$. However the finesse of the details within the swirls, suggest a level of detailed plasma interaction well below that of the proton dynamics scale.

This is quantified by determining the characteristic scale length of the magnetic inhomogeneity/magnetic anomaly $\widetilde{\lambda}_B = [(1/B)(dB/dh)]^{-1}$. Here $\widetilde{\lambda}_B$ is $\sim 1km$, assuming a surface magnetic field B of 200nT and the boundary to be at an altitude, h, of $20km$.

This means the protons are effectively unmagnetized [65].

Conversely the electrons gyro radius is small compared to the overall size of the structure that they are able to follow the abrupt changes in magnetic field created by the solar wind interacting with the magnetic anomaly and diamagnetic cavity. The difference in behaviour between the magnetized electrons and unmagnetized protons sets up a space charge electric field that controls the protons behaviour [66, 67]. This occurs not just at the lunar surface but throughout the mini-magnetosphere boundary. In order to model this scale of interaction these criteria must be maintained between lunar, laboratory [50, 68] and computer simulation. Only a full plasma kinetic code [2, 69] can capture these characteristics.

THE SIMULATIONS

The simulation was carried out using a plasma particle-in-cell (PIC) code [69] called OSIRIS [2]. In the OSIRIS code the full set of Maxwells equations are solved on a grid using currents and charge densities calculated by weighting discrete particles onto the grid. Each particle is pushed to a new position and momentum via self-consistently calculated fields. The code makes few physics approximations and is ideally suited for studying complex systems with many degrees of freedom such as this one. The reason this is necessary is that the scale size of the mini-magnetosphere structure is very much smaller than the magnetohydrodynamic (MHD) code allows. No filtering is performed in these simulations. This allows us to resolve plasma waves in space and time including whistler waves [42, 43]. The code is a time and space domain code, not a spectral code, so the equations are integrated via fast Fourier transforms.

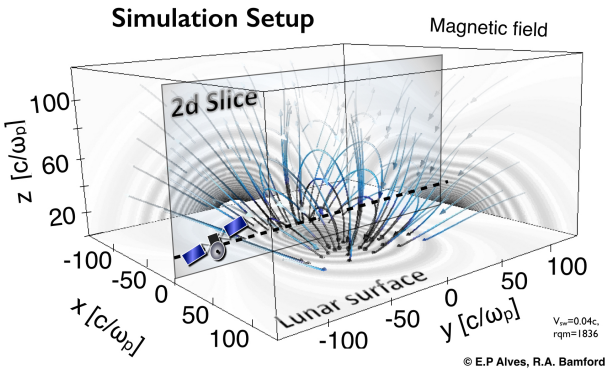

FIG. 2: The geometry of the simulation. The lunar surface is represented by the lower $x-z$ plane. A single source magnetic dipole is placed just below and parallel to the $x-z$ plane, with the magnetic axis aligned along $x=0$, with the north pole orientated in the $+z$ direction. The result is a hemispherical magnetic field emerging from the surface. The magnetic field intensity is shown projected onto the back walls and ground plane in banded grey where decreasing band interval correspond to increasing magnetic field intensity. A magnetised 'solar wind' plasma with density n_{sw} and magnetic field B_{sw} (antiparallel to anomaly field) is introduced from the top plane with a flow velocity $-\mathbf{v_{sw}}$ vertically down onto the lunar surface. Selected magnetic field lines are shown in graduated blue. The magnetic dipole moment $\mathbf{m_m}$ is 25 normalized units long and resides 25 units below the center of the box aligned with the positive $\mathbf{x}$ axis. The plane marked '2D slice' shows the relative orientation of the sections shown in Figures 4(a). The dashed line on the 2D section represents the path of a conceptual spacecraft sampling the parameters results of which are shown in Figures 4(b) and 6(a). The simulation code operates in normalised plasma units with the independent variable being n_{sw}. The proton to electron charge to mass ratio used is the realistic value of 1836.

The simulations setup is shown in Figure 2 together with a dipole field whose axis is **parallel to** the plane of the surface. Full 3D simulations results in Figure 3, show the magnetic field structure, electric field and proton orbits self-consistently derived.

Table I shows a summary of the 3D simulation parameters used and their relationship to typical observational values (based on [41]).

In order to maintain dynamic similarity [71–73] with the lunar environment, the magnetic fields and temperatures were normalized proportionately so as to maintain the same control variables of plasma β (thermal pressure to magnetic pressure) and M_m (magnetosonic mach numbers and speeds).

The simulation code is used here to recreate simplified

TABLE I: A table of the plasma parameters values used in the 3-D simulation.

Plasma Parameter	**Symbol**	**Value**
Plasma Temperature	T_i	5 eV
Plasma Density	n_{sw}	10 cm^{-3}
Solar Wind flow velocity*	v_{sw}	600 kms^{-1}
Solar Wind Magnetic field*	B_{sw}	10 nT
Debye length	λ_D	0.01 km
Thermal proton Larmor orbit	$r_{L,i,th}$	97 km
Flow proton Larmor orbit	$r_{L,i,fl}$	627 km
Electron Larmor radius	r_{Le}	1 km
Electron Skin depth	c/ω_{pe}	1.7 km
Ion Skin depth	c/ω_{pi}	97 km
Magnetic field at stand-off*†	$\lvert B(r_s)\rvert$	120 nT
Magnetosonic Mach	M_m	8
Plasma beta	β	0.2
Ratio ion-electron charge–to–mass	rqm	1836
Simulation Box size		$340 \times 340 \times 170$ km
Grid resolution		300 m

*Operationally for computational speed plasma inflow and source magnetic field both increase by factor $F=20$ which maintained pressure balance $B^2/2\mu_o = n_{sw}mv_{sw}^2/2$ at stand-off altitude of $r_s = c/\omega_{pi}$.

case study combinations of plasma parameter conditions and magnetic field dipole orientations and intensities. These can be compared to the analytical expressions[50] and observational data e.g.[40] for mini-magnetospheres.

Figure 3 shows the results of the simulation of the solar wind plasma impacting a localised crustal magnetic field structure. Insert is a photograph of the Reiner Gamma lunar swirl taken by KAGUYA [70] spacecraft. This particular image is at an inclined angle similar to the simulation image's orientation to the representative plane of the 'lunar surface' allowing a comparison of the footprint deposition of protons (red) in the simulation and the "white" of the lunar swirl.

In Figure 3 only the proton density above a threshold is visualised in order to make the box transparent. The magnetic field structure is shown by the blue field lines (again in-part omitted for sake of clarity). The red represents the space-charge electric field at the boundary, which is set up by the different penetration depths between protons and electrons at the edge of the magnetosphere. The lateral-projections of the electric field structure (corresponding also to the relative proton density) reveal interesting dynamic features and orthogonal asymmetries. The projection on the $y-z$ plane shows a rippled surface structure, due to the diamagnetic electron-ion drift instability which occurs perpendicular to the magnetic field lines [22]. In contrast, the projection on the $x-z$ plane shows a smooth surface structure since the relative electron-ion drift is absent. This illustrates the anisotropic preferences of particular plasma instabil-

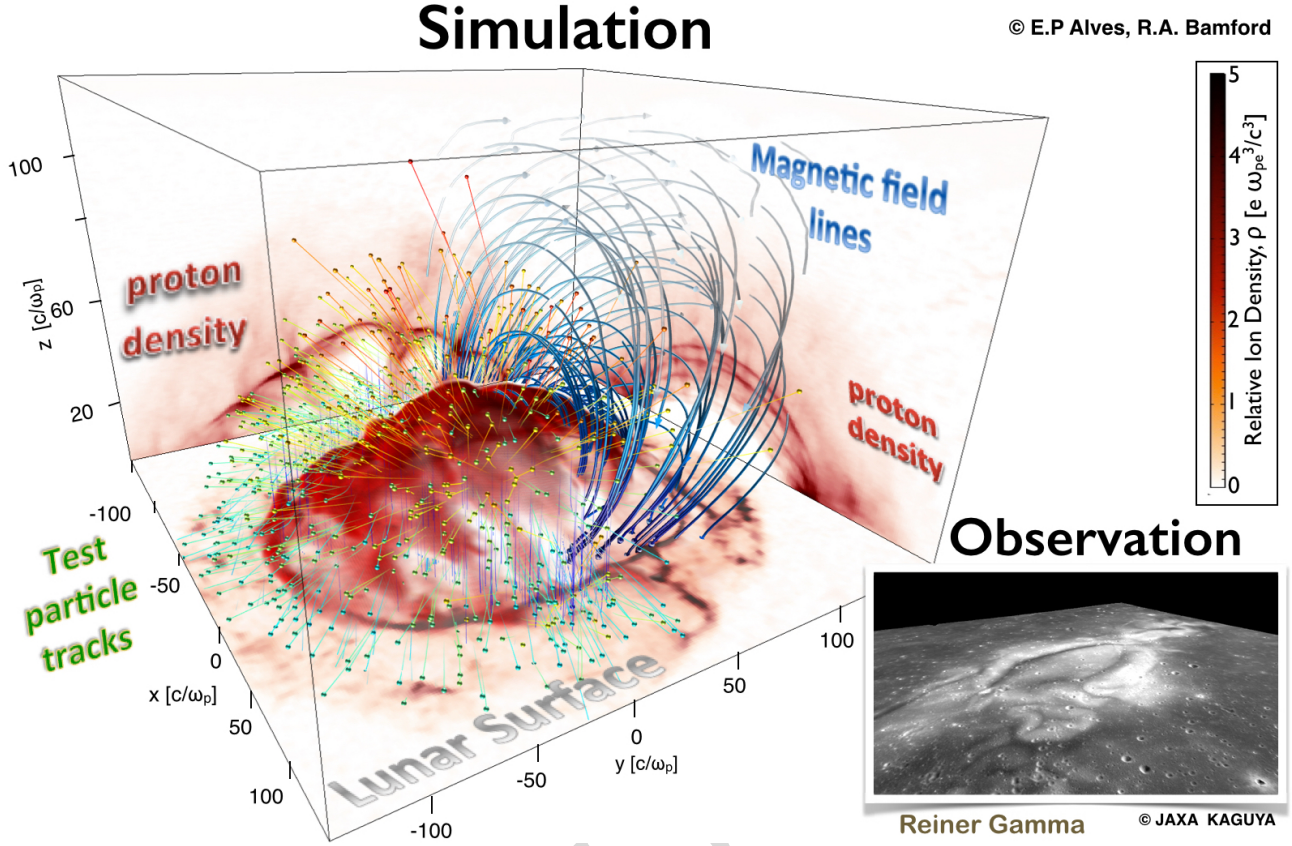

FIG. 3: (Colour) A 3D magnetized plasma collision with a surface magnetic dipole. Insert: A low altitude, inclined angle photograph taken by the JAXA KAGUYA [70] spacecraft of the Reiner Gamma Formation as an example of a lunar swirl albedo anomaly located co-incident with the a localised crustal magnetic field. The solar wind plasma (flowing vertically downwards) impacts a localised crustal magnetic field structure (blue lines). The green spheres and tracks show a subset of protons population trajectory being scattered from the narrow polarisation electric field (red). Proton density enhancements follow the electric field. Only part of the magnetic field lines are shown for clarity and the background densities are not visualised. Superficial similarities of form and 'wisp-like' structures in the lunar swirl patten as present in the pattern of the proton (red) deposition on the surface plane in the simulation.

ities. However the narrow width of the barrier remains a consistent feature, although not necessarily a single, smooth boundary due to waves, turbulence and instabilities - the magnitude of which alter with specific conditions. Representative trajectories of a few solar wind protons are shown by the small spheres and yellow track lines and are seen to be widely scattered not by a gradual redirection but ballistically scattered from a very narrow region close to the surface. The electric field responsible for scattering can be seen to be omni-directionally pointing outwards regardless of the magnetic field orientation. This is because it is proportional to the *gradient* in the magnetic field intensity $\nabla|B|^2$ not $|\mathbf{B}|$ in accordance with theoretical expectations [50]. The projection onto the $x-z$ or surface plane, shows the electric field intensity at the lunar surface. The proton density is controlled, on these scales, by the electric field rather than the magnetic field because the protons are unmagnetised. The simulation shown in Figure 3, therefore, shows the distribution of sharp regions of enhanced proton-flux and regions of depleted proton flux.

2D cut-throughs of 3D simulation

In order to reveal the details of the interior structures of the 3D simulation Figure 4 shows the 2 dimensional sections of each of the plasma parameters. These are from top to bottom the proton and electron density n_i, n_e, the resultant electric E and magnetic field B and the original dipole magnetic field undisturbed by the solar wind plasma B_{dipole}. The plane of the section bisects the midpoint in x of the dipole axis and is indicated in Figure 2. Figure 4 shows the simulated plasma instrument signatures for the specific altitude ($20 \times c/\omega_{pe} = 34\ km$ for plasma density of 10 cm^{-3}) indicated in the previous figures (4 to 9). Clearly a flight path at different altitude, orientation and conditions will alter the plots

(some of which will be shown later). However this example from a single dipole contains all the basic component features of the double layers of the barrier going in and out of the cavity.

The density pile-ups, exclusion of the majority of the particles from the interior, back-flow and turbulence of the barrier are apparent on all parameters. The barrier that forms results in responsive inductive currents and corresponding magnetic fields. The thickness of the barrier is of the order of the electron skin depth $\sim c/\omega_{pe}$, as theoretically predicted [50]. The small-scale plasma instabilities, waves and turbulence formed, provide the means by which the proton and electron particle distributions become non-thermal and exchange energy through Landau damping [67]. This is illustrated in the top two panels of Figure 4 discussed in Section .

The "stand-off" distance, r_s [50] that the magnetic cavity reaches force balance with the incoming plasma. For a cavity to be evident requires that r_s be greater than the barrier width/electron skin depth. Most important is the intensity of magnetic field *at the magnetopause*. The placement of the reference 'lunar surface' plane can go up or down making reference to a surface magnetic field intensity dependant on choice of distance from the magnetopause. These simulations show that a magnetic field intensity of $< 300nT$ would be sufficient to produce a "mini-magnetosphere" for a density 10 cm^{-3}.

Simulating Spacecraft flyover signatures

Figure 4 shows how the simulation results translate as observations from a spacecraft flying above the surface anomaly.

These features should be common to any mini-magnetosphere to some degree or another irrespective of the presence of lunar swirls. The comparison is qualitative not quantitive to highlight the nature of interplay in the parameters so as to provide identification of phenomena between theory and observation via simulation visualisation.

Particle distributions and kinetic instabilities

In a previous paper [50], in-situ satellite data, theory and laboratory validation showed that it is an electric field associated with the small scale collisionless shock that is responsible for reflecting, slowing and deflecting the incoming solar wind around mini-magnetospheres. It was shown that the electric field of polarization, caused by the gradient in the magnetic field, between charge carriers of the solar wind flow, is of prime importance. This polarization field leads to reflection and scattering of the protons and electrons [74]. The counter-streaming of the protons ahead of the barrier is responsible for generating lower-hybrid waves via the modified two-stream instability [75]. The electric potential component, ϕ, responsible for slowing and deflecting the protons [50] is:

$$\phi = -(1/2\mu_0 ne).B_z^2.$$

For a density of $\sim 5cm^{-3}$ and a magnetic field $B_z \sim 30 \times 10^{-9}T$ (similar to those observed at the pile-up reported by Lunar Prospector [76]), provides a theoretical value of $\phi_{theory} \sim 450V$ [50], similar to the $\phi_{obs} \sim 400V$ [36]. The value for these simulations for $n = 10cm^{-3}$ is $\delta E \approx 300V$.

The plasma wave turbulence is identified to be close to the lower hybrid frequency $= (\omega_{ce}\omega_{ci})^{1/2}$, where ω_{ce} and ω_{ci} are the electron and proton cyclotron frequencies respectfully, agreeing with data from spacecraft that observed intense lower hybrid electrostatic oscillations of the order of 1-10 Hz [77]. The lower-hybrid waves generated by the modified two stream instability previously reported by [74] and shown to be responsible for the electron acceleration also is observed by the satellites.These waves are also present at other collisionless shocks e.g.[78–80].

The counter streaming protons produced by encountering the electric field result in modifications to the proton particle distributions. Figure 5 shows an analysis of the vertical component of the proton momentum ($p_{z,i} = m_p v_{zi}$) from the 3D simulation shown in previous figures. Top left of the figure shows the magnitude of the vertical component of the proton momentum (a proxy for vertical kinetic energy), against altitude z (in dimensionless units of $c/\omega_{pe} = 1.7km$ for a density of $10 \times 10^6 m^{-3}$). Shown below are examples of the proton distribution functions for selected altitudes of $z = 20, 60$ and $100c/\omega_{pe}$. These represent examples of distribution functions that could be expected to be encountered by a spacecraft passing (A) below the magnetopause barrier, (B) just above the barrier and (C) in the 'foot' region upstream of the encounter. The incoming proton stream has a narrow (cold) distribution at -0.04c, and is flowing from right (high z) to left (low z). As the inflow particles encounters the mini-magnetosphere boundary (at about $z = 55$), the distributions alter. Comparing the form of distribution functions for the vertical momentum at different altitudes shows the formation of a 'bump-on-tail' distribution. The variation with altitude illustrates how observational spectra, such as that observed by non-thermal protons observed by Nozomi [77] at an altitude of 2800 km, are consistent with the simulation and the different spectra observed at lower altitudes an example of which is shown in the insert labelled (b) "Observations" in Figure 5 (from [44]). A similar comparison can be seen in Figure 5(right) for the electrons. The widening of the vertical momentum component seen in the simulation plot (lower panel) coincides with encountering the barrier region and corresponds to a temperature increase. Together the proton and electron spectra in Figure 5 show that the non-adiabatic exchanges between

the particle species are present in both observations and simulations.

The level of detail in the momentum spectra is indicative of the ability of the fully self-consistent simulation code to represent the kinetic instabilities. These can be seen in the periodic structures (such as those seen $p_z < -0.05$). The 'finger-like' structures in the counter streaming population $z > 60$ to 120 and $p_z > 0.0$ to 0.05 are indications of waves formed as a result of the modified two stream instability [74, 81]. These results are also seen in PIC simulations of collisionless shocks of planetary magnetosphere (for example [45–49].

Comparison with lunar swirls

A complicated magnetic footprint, that is limited in extent and isolated was observed by the SARA instument on Chandrayaan-1 [33, 82, 83] (at 22°S and 240°E on the lunar farside, and shown in left hand 2 panels of Figure 6). Such a structure would appear in the far-field as a single dipole similar to that used in the simulation (shown in right hand panels of Figure 6). The simulation reproduces a wider enhanced ring region about the central void in the relative proton density spacial distribution in the vicinity of the dipole magnetic field. The static instance and higher resolution of the simulation compared to the observation, allows the narrow electron scale barrier and wider pre-transition region, to be distinguished. The density variations due to kinetic scale instabilities and turbulence are also resolved for a moment frozen in time. In space the variations in space weather conditions would randomise, widen and reduce, as well as introduce asymmetries to the proton spatial distribution. Nevertheless the simulation illustrates the principles at play and that the determining force controlling the protons is the pondermotive (or energy density gradient) force.

Simulated relative proton flux with dark lanes and lunar swirls

The relative proton density from the simulation can be further clarified by examining a linear plot taken at the equivalent lunar surface level. This is shown in Figure 6.

If sustained long term, this pattern of excluded and narrow enhance proton density resulting from the action of the mini-magnetosphere with crustal magnetic field would be consistent with the distribution and finesse required to form the variety of lighter and darker albedo alterations seen in lunar swirls [62].

The relative deposition of proton flux (shown in grey) on the surface slice from the simulation is shown in the top left image of Figure 8 with the magnetic field lines of the dipole. This is compared to an image of the central region of the most distinctive example of a lunar swirl, Reiner Gamma Formation located at $7.4°N, 300.9°E$, taken by NASA's Lunar Reconnaissance Orbiter [84]. The agreement between the key characteristics of dark lane [85] width and shielded interior can be seen to be totally consistent.

We will now preform a series of simulations to study the parameter regime of single dipoles by varying the orientation and some of the plasma conditions.

PARAMETRIC ANALYSIS (USING 2D SIMULATIONS)

In the following section a brief exploration of how: (a) dipole orientation relative to the lunar surface, (b) environmental plasma Alfvén Mach number and parallel or anti-parallel, (c) changes in the surface dipole effective magnetic field intensity and range, affect the results of the simulation and hence the observed signatures. As the parametric analysis shown here is only intended to provide an indication of the relative significance of major parameter changes, a 2D simulation is sufficient.

The effect of dipole orientation

Changing the orientation of the emerging magnetic dipole relative to the surface plane produces the same diamagnetic characteristics of narrow barrier, particle reflection, cavity formation, waves and turbulence. However, as can be seen in Figure 9, the overall morphologies of the relative proton distribution are very different.

Figure 9 (a) shows 2D simulations of the same magnetic dipole in 3 orthogonal directions $\mathbf{x}, \mathbf{y}$ and $\mathbf{z}$, relative to the surface plane. The solar wind, mass ratio and plasma conditions are as those of the 3D simulation with the exception that the solar wind has no magnetic field. The consequence of $\mathbf{B_{sw}}$ parallel or antiparallel to the surface magnetic field is shown in the next section.

The effects of changes in the environmental plasma

Although the crustal magnetic anomalies are a fixed magnetic field source, the plasma environment is not. There are periodicities due to orbits and diverse solar wind and/or magnetospheric conditions. Through simulation this can be explored in Figures 9(b) and (c).

A qualitative comparison of the variation of mini-magnetosphere characteristics in Figure 9(b) shows that anti-parallel field creates larger cavities and that the width turbulent layer varies considerably as does proton pick-up. The higher magnetosonic Mach number compresses the turbulence region sharpens up the transition as well as reduces the cavity size. The comparison also

illustrates how a spacecraft passing at the same altitude will observe very different conditions. A more oblique angle for the direction of the plasma flow will also multiply the number of combinations that could be recorded for the same magnetic field source.

A spacecraft passing over the vicinity of these anomalies, at a fixed height (as indicated in the Figures by a satellite graphic and dashed 'flight-path' line) but under the different plasma conditions will sometimes transect the different regions of a mini-magnetosphere and so observe different characteristics. (An illustration of these plasma data instrumentation signatures in such a flyover is shown in Figure 4).

Figures 9 (b) and 9(b) illustrate the consequence of combinations of changes in the simulation conditions. In Figure 9(a), the incoming solar wind magnetosonic mach numbers M_m and parallel (or anti-parallel) solar wind magnetic field $\mathbf{B_{sw}}$ orientation are varied. In Figure 9(c) the dipole size/length, L_{dipole}, is altered. The extent of the dipole can be altered either through being a larger single crustal magnetic field or by multiple smaller conglomerations (such as on the far-side of the Moon) that will appear as a single dipole when observed in sufficient altitude to be in the far-field. If two regions of magnetic anomalies are sufficiently far apart then they would appear as two dipoles and so on. The complexity of the near field, ground level magnetic topology cannot readily be identified from space due to the interaction of the original magnetic field and the environmental plasma that is creating in-situ currents, electric fields and compensating local magnetic variations at or near the altitude of the spacecraft flyover. For this reason simulating a distribution of magnetic dipoles over the surface can provide equally valid answers.

In all these figures the white-to-red colour distribution represents relative proton density and all the conditions are the same except for those stated as otherwise.

In summary, the 2D simulations show how only occasionally might certain features, like the diamagnetic cavity, be clearly detected in in-situ instrumentation, such as particle detectors and magnetometers. This is especially true for a rapid spacecraft transit through very small isolated magnetic field anomalies. However, other instrumentations such as imagers[33], that look down onto the features could still detect the characteristic depletion in proton reflection.

CONCLUSIONS

In this paper, for the first time, results are shown from a fully self-consistent 3D particle–in–cell simulation, side–by–side with in–situ observations from several lunar satellites investigating lunar magnetic anomalies. The conditions used in the pic simulation are consistent with actual conditions. These simulations show that a magnetic field intensity of $< 300nT$ is sufficient to produce a "mini-magnetosphere" with collisionless shock and diamagnetic cavity, for a solar wind density of 10 cm^{-3} with a $10nT$ interplanetary magnetic field, flowing at 600 kms^{-1} - a magnetosonic Mach number of 8.

We have demonstrated, for the first time, that collisionless shocks can form at sub-proton Larmor orbit dimensions.

All of the observational characteristics identified as being associated with lunar mini-magnetospheres, are accounted for in the comparison. This includes, in particular, the origin of the dark lanes of the lunar swirls in agreement with the spectroscopic observations of lunar surface albedo [1, 3, 58, 61, 64, 86]. The in-situ observations from plasma instrumentation on board satellites at altitudes from $10 - 1000s$ km includes; magnetic and density pile up, back-flow, narrow electrostatic barrier, solitary and lower hybrid waves, turbulence spectrum, Whistlers, cavity formation, beams, particle pick-up, electron heating, ion slowing, reflection and deflection. The 3D simulation has reproduced all these using the simplest of magnetic topologies - a single magnetic dipole. The single dipole represents an archetype. It can be both the far–field resultant magnetic structure of conglomerations of random surface fields, as well as representing a component part of a more complicated distributed near–field surface magnetic field topology.

It is shown in this paper, how the different orientations and plasma conditions alter the archetype. The magnetic fields simulated are modest, $100s$ of nT for realistic solar wind flow velocities $\sim 100s$ kms^{-1}, densities $\sim 1 - 100$ cm^{-3}, plasma $\beta < 1$, realistic charge–to–mass ratios and Alfvèn Mach numbers $2 - 8$.

In all orientations, a narrow electrostatic field forms at the locations where the magnetic field and particle densities pile-up. The magnitude of the electrostatic field is proportional to the *gradient* in magnetic field in accordance with theory and laboratory experiments [50]. This occurs as a result of the impacting plasma environments (the solar wind plasma and the plasma in and immediately around the fixed footprint of the surface magnetic field). The thickness of this barrier is approximately equal to the electron skin depth c/ω_{pe} (where ω_{pe} is the electron plasma frequency) in agreement with theory for collisionless shocks [87].

The 3D simulation was of a dipole whose magnetic axis was parallel to the surface but buried below it. Being 3D it showed how the outwardly pointing, narrow electrostatic field formed in every orientation resulting in a protective 'dome' that scattered the incoming protons thereby reducing the proton flux reaching the lunar surface. The dome was compressed by the solar wind pressure resulting in a spreading of the dipole mid-plane, parallel to the surface magnetic field lines. At the edges of the dome, the narrow, electrostatic sheath, intersected the lunar surface producing a means of channelling a

higher proportion of the impacting proton flux into narrow regions or 'lanes' around the edge of the protected dome. The width of these enhanced proton outlines are of the order of the electron dynamics (kilometre or less) and look in form and width very similar to the "dark lanes" of the lunar swirls. Similar electron scale plasma filamentations occurred at the poles –which were laid horizontally in the 3D example used here.

Together this provides support for the hypothesis that the observed spectral effects resulting in the lunar swirls are due to differential proton bombardment. One prediction of this work is that the dark lanes width will be the same for any of the lunar swirls distributed about the moon whether they are in either large conglomerations or isolated patches.

ACKNOWLEDGEMENTS

The authors would like to thank Science and Technology Facilities Physics for Fundamental Physics and Computing resources provided funding by STFC's Scientific Computing Department, the European Research Council (ERC 2010 AdG Grant 267841) and FCT (Portugal) grants SFRH/BD/75558/2010 for support. We acknowledge PRACE for awarding access to the supercomputing resources SuperMUC and JUQUEEN based in Germany.

* Ruth.Bamford@stfc.ac.uk
† Also at Central Laser Facility, STFC, Rutherford Appleton Laboratory, Chilton, Didcot, OX11 0QX, UK.

[1] C. Pieters, E. Fischer, O. Rode, and A. Basu, Journal of Geophysical Research: Planets (1991–2012) **98**, 20817 (1993).
[2] R. Fonseca, L. Silva, F. Tsung, V. Decyk, W. Lu, C. Ren, W. Mori, S. Deng, S. Lee, T. Katsouleas, *et al.*, Computational Science—ICCS 2002 , 342 (2002).
[3] G. Y. Kramer, S. Besse, D. Dhingra, J. Nettles, R. Klima, I. Garrick-Bethell, R. N. Clark, J.-P. Combe, J. W. Head III, L. A. Taylor, *et al.*, Journal of Geophysical Research **116**, E00G18 (2011).
[4] E. F. Lyon, H. S. Bridge, and J. H. Binsack, Journal of Geophysical Research **72**, 6113 (1967).
[5] P. Dyal, C. W. Parkin, and C. P. Sonett, Science **169**, 762 (1970).
[6] P. Coleman, B. Lichtenstein, C. Russell, L. Sharp, and G. Schubert, "Magnetic fields near the moon," (1972).
[7] L. Hood and G. Schubert, Science **208**, 49 (1980).
[8] N. Richmond, L. Hood, J. Halekas, D. Mitchell, R. Lin, M. Acuna, and A. Binder, Geophys. Res. Lett **30**, 1395 (2003).
[9] L. L. Hood and N. A. Artemieva, Icarus **193**, 485 (2008).
[10] J. Halekas, D. Mitchell, R. Lin, S. Frey, L. Hood, M. Acuna, and A. Binder, Journal of Geophysical Research. E. Planets **106**, 27 (2001).
[11] M. Acuna, J. Connerney, R. Lin, D. Mitchell, C. Carlson, J. McFadden, K. Anderson, H. Rème, C. Mazelle, D. Vignes, *et al.*, Science **284**, 790 (1999).
[12] L. V. Starukhina and Y. G. Shkuratov, Icarus **167**, 136 (2004).
[13] M. Kivelson, Z. Wang, S. Joy, K. Khurana, C. Polanskey, D. Southwood, and R. Walker, Advances in Space Research **16**, 59 (1995).
[14] L. Gargaté, R. Bingham, R. Fonseca, R. Bamford, A. Thornton, K. Gibson, J. Bradford, and L. Silva, Plasma Physics and Controlled Fusion **50**, 074017 (2008).
[15] R. A. Bamford *et. al.*, Plasma Phys. and Cont. Fus. **50**, 741 (2008).
[16] A. Poppe, J. Halekas, G. Delory, and W. Farrell, Journal of Geophysical Research: Space Physics (1978–2012) **117** (2012).
[17] E. Kallio, R. Jarvinen, S. Dyadechkin, P. Wurz, S. Barabash, F. Alvarez, V. A. Fernandes, F. Yoshifumi, A.-M. Harri, J. Heilimo, *et al.*, Planetary and Space Science (2012).
[18] R. Bamford, E. Alves, B. Kellett, W. Bradford, L. Silva, I. Crawford, R. Trines, K. Gibson, A. Thornton, R. Fonseca, *et al.*, LPI Contributions **1719**, 1292 (2013).
[19] R. Bamford, E. Alves, B. Kellett, W. Bradford, L. Silva, I. Crawford, R. Trines, R. Fonseca, L. Gargate, and R. Bingham, in *European Planetary Science Congress 2013, held 8-13 September in London, UK. Online at: http://meetings. copernicus. org/epsc2013, id. EPSC2013-542*, Vol. 8 (2013) p. 542.
[20] J. Deca, A. Divin, G. Lapenta, B. Lembège, S. Markidis, and M. Horányi, Physical review letters **112**, 151102 (2014).
[21] R. Jarvinen, M. Alho, E. Kallio, P. Wurz, S. Barabash, and Y. Futaana, Geophysical Research Letters **41**, 2243 (2014).
[22] F. Cruz, E. Alves, R. Bamford, R. Bingham, R. Fonseca, and L. Silva, European Physical Society, Plasma Physics Conference, July 2015 (2015).
[23] R. Bamford, E. Alves, F. Cruz, B. Kellett, R. Fonseca, L. Silva, R. Trines, J. Halekas, G. Kramer, E. Harnett, R. Cairns, and R. Bingham, (2015), arXiv:1505.06304v1.
[24] J. Deca, B. Divin A, Lembège, M. Horányi, S. Markidis, and G. Lapenta, J. Geophys. Res. Space Physics , 120 (2015).
[25] S. Fatemi, C. Lue, M. Holmström, A. R. Poppe, M. Wieser, S. Barabash, and G. T. Delory, Journal of Geophysical Research: Space Physics (2015).
[26] S. Dyadechkin, E. Kallio, and P. Wurz, J. Geophys. Res. Space Physics **120**, 15891606 (2015).
[27] F. Cruz, E. Alves, R. Bamford, R. Bingham, R. Fonseca, and L. Silva, Submitted to Physics of Plasmas (2016).
[28] E. M. Harnett and R. M. Winglee, Journal of geophysical research **107**, 1421 (2002).
[29] E. M. Harnett and R. M. Winglee, Journal of geophysical research **108**, 1088 (2003).
[30] M. Kurata, H. Tsunakawa, Y. Saito, H. Shibuya, M. Matsushima, and H. Shimizu, Geophysical research letters **32** (2005).
[31] R. Lin, D. Mitchell, D. Curtis, K. Anderson, C. Carlson, J. McFadden, M. Acuna, L. Hood, and A. Binder, Science **281**, 1480 (1998).
[32] M. Wieser *et. al.*, Planetary and Space Sci. **57**, 2132 (2009).

[33] M. Wieser, S. Barabash, Y. Futaana, M. Holmström, A. Bhardwaj, R. Sridharan, M. Dhanya, A. Schaufelberger, P. Wurz, and K. Asamura, Geophysical Research Letters **37**, L05103_1 (2010).

[34] S. Huixian, D. Shuwu, Y. Jianfeng, W. Ji, and J. Jingshan, Journal of earth system science **114**, 789 (2005).

[35] K. Hashimoto *et al.*, Geophys. Res.Lett. **37**, L19204 (2010).

[36] Y. Futaana, S. Barabash, M. Wieser, M. Holmström, A. Bhardwaj, M. Dhanya, R. Sridharan, P. Wurz, A. Schaufelberger, and K. Asamura, J. of Geophys. Res. **115**, A10248 (2010).

[37] C. Lue, Y. Futaana, S. Barabash, M. Wieser, M. Holmström, A. Bhardwaj, M. Dhanya, and P. Wurz, Geophysical Research Letters **38**, L03202 (2011).

[38] X. Wang, M. Horányi, and S. Robertson, Journal of Geophysical Research **117**, A06226 (2012).

[39] S. Yokota, Y. Saito, K. Asamura, M. N. Nishino, T. I. Yamamoto, H. Tsunakawa, H. Shibuya, M. Matsushima, H. Shimizu, F. Takahashi, *et al.*, Planetary and Space Science **93**, 87 (2014).

[40] J. Halekas, A. Poppe, J. McFadden, V. Angelopoulos, K.-H. Glassmeier, and D. Brain, Geophysical Research Letters **41**, 7436 (2014).

[41] N. J. Edberg, M. Lester, S. Cowley, D. Brain, M. Fränz, and S. Barabash, Journal of Geophysical Research: Space Physics (1978–2012) **115** (2010).

[42] J. Halekas, D. Brain, D. Mitchell, and R. Lin, Geophysical research letters **33** (2006).

[43] T. Nakagawa, F. Takahashi, H. Tsunakawa, H. Shibuya, H. Shimizu, and M. Matsushima, Earth, planets and space **63**, 37 (2011).

[44] Y. Saito, M. N. Nishino, M. Fujimoto, T. Yamamoto, S. Yokota, H. Tsunakawa, H. Shibuya, M. Matsushima, H. Shimizu, and F. Takahashi, Earth Planets Space **64**, 83 (2012).

[45] D. Forslund and J. Freidberg, Physical Review Letters **27**, 1189 (1971).

[46] D. Forslund, K. Quest, J. Brackbill, and K. Lee, Journal of Geophysical Research: Space Physics (1978–2012) **89**, 2142 (1984).

[47] K. Quest, Journal of Geophysical Research: Space Physics (1978–2012) **93**, 9649 (1988).

[48] R. Blandford and D. Eichler, Physics Reports **154**, 1 (1987).

[49] H. Kucharek and M. Scholer, Advances in Space Research **15**, 171 (1995).

[50] R. Bamford, B. Kellett, W. Bradford, C. Norberg, A. Thornton, K. Gibson, I. Crawford, L. Silva, L. Gargaté, and R. Bingham, Physical Review Letters **109**, 81101 (2012).

[51] I. Garrick-Bethell *et. al.*, Icarus **212**, 480 (2011).

[52] F. El-Baz, in *Lunar and Planetary Science Conference Proceedings*, Vol. 3 (1972) p. 39.

[53] L. Hood and C. Williams, in *Lunar and Planetary Science Conference Proceedings*, Vol. 19 (1989) pp. 99–113.

[54] D. T. Blewett *et. al.*, J. Geophys. Res. **116**, 1 (2011).

[55] F. El-Baz, A. Worden, and V. Brand, in *Lunar and Planetary Science Conference*, Vol. 3 (1972) p. 219.

[56] J. F. Bell and B. R. HAWKE, Publications of the Astronomical Society of the Pacific , 862 (1987).

[57] P. C. Pinet, V. V. Shevchenko, S. D. Chevrel, Y. Daydou, and C. Rosemberg, Journal of Geophysical Research: Planets (1991–2012) **105**, 9457 (2000).

[58] D. Blewett, B. Hawke, N. Richmond, and C. Hughes, Geophysical Research Letters **34**, L24206 (2007).

[59] P. H. Schultz, L. J. Srnka, S. Pai, and S. Menon, in *Lunar and Planetary Science Conference*, Vol. 11 (1980) pp. 1009–1011.

[60] I. Garrick-Bethell, J. W. Head, and C. M. Pieters, Icarus **212**, 480 (2011).

[61] T. D. Glotch, J. L. Bandfield, P. G. Lucey, P. O. Hayne, B. T. Greenhagen, J. A. Arnold, R. R. Ghent, and D. A. Paige, Nature communications **6** (2015).

[62] E. M. Harnett and G. Y. Kramer, Submitted to Annales Geophysicae (2015).

[63] N. Richmond and L. Hood, Journal of Geophysical Research **113**, E02010 (2008).

[64] G. Y. Kramer, J.-P. Combe, E. M. Harnett, B. R. Hawke, S. K. Noble, D. T. Blewett, T. B. McCord, and T. A. Giguere, Journal of Geophysical Research **116**, E04008 (2011).

[65] I. Langmuir, Physical Review **33**, 954 (1929).

[66] N. Borisov and U. Mall, Physics Letters A **309**, 277 (2003).

[67] R. Bingham, *Plasma Physics: An Introductory Course*, edited by R. Dendy (Cambridge University Press, 1993).

[68] R. Bamford, K. Gibson, A. Thornton, J. Bradford, R. Bingham, L. Gargaté, L. Silva, R. Fonseca, M. Hapgood, C. Norberg, *et al.*, Plasma Physics and Controlled Fusion **50**, 124025 (2008).

[69] J. M. Dawson, Reviews of modern physics **55**, 403 (1983).

[70] M. Kato, S. Sasaki, and Y. Takizawa, Space science reviews **154**, 3 (2010).

[71] J. Lacina, Plasma Physics **13**, 303 (1971).

[72] J. Connor, Plasma physics and controlled fusion **30**, 619 (1988).

[73] D. Ryutov, R. Drake, and B. Remington, The Astrophysical Journal Supplement Series **127**, 465 (2000).

[74] R. Bingham, R. Bamford, B. Kellett, and V. Shapiro, Journal of Plasma Physics **76**, 915 (2010).

[75] J. B. McBride, E. Ott, J. P. Boris, and J. H. Orens, Physics of Fluids **15**, 2367 (1972).

[76] R. P. Lin *et. al.*, Science **281**, 1480 (1998).

[77] Y. Futaana, S. Machida, Y. Saito, A. Matsuoka, and H. Hayakawa, J. Geophys. Res **108**, 1025 (2003).

[78] A. Balogh and R. A. Treumann, *Physics of collisionless shocks: space plasma shock waves* (Springer Science & Business Media, 2013).

[79] P. Ghavamian, J. M. Laming, and C. E. Rakowski, The Astrophysical Journal Letters **654**, L69 (2006).

[80] B. T. Tsurutani, *Collisionless shocks in the heliosphere: Reviews of current research* (American Geophysical Union, 1985).

[81] M. E. Dieckmann, B. Eliasson, P. K. Shukla, N. J. Sircombe, and R. O. Dendy, Plasma physics and controlled fusion **48**, B303 (2006).

[82] Y. Futaana, S. Barabash, M. Wieser, C. Lue, P. Wurz, A. Vorburger, A. Bhardwaj, and K. Asamura, Geophysical Research Letters (2013).

[83] A. Vorburger, P. Wurz, S. Barabash, M. Wieser, Y. Futaana, M. Holmström, A. Bhardwaj, and K. Asamura, Journal of Geophysical Research **117**, A07208 (2012).

[84] `http://lroc.sese.asu.edu/posts/575`.

[85] J. F. Bell and B. R. Hawke, in *Lunar and Planetary Science Conference Proceedings*, Vol. 12 (1982) pp. 679–694.

[86] L. A. Taylor, C. M. Pieters, L. P. Keller, R. V. Morris, and D. S. McKay, Journal of Geophysical Research:

Planets (1991–2012) **106**, 27985 (2001).

[87] D. Tidman and N. A. Krall, *Shock Waves in Collisionless Plasmas*, edited by S. C. Brown (Wiley and Sons, 1971).

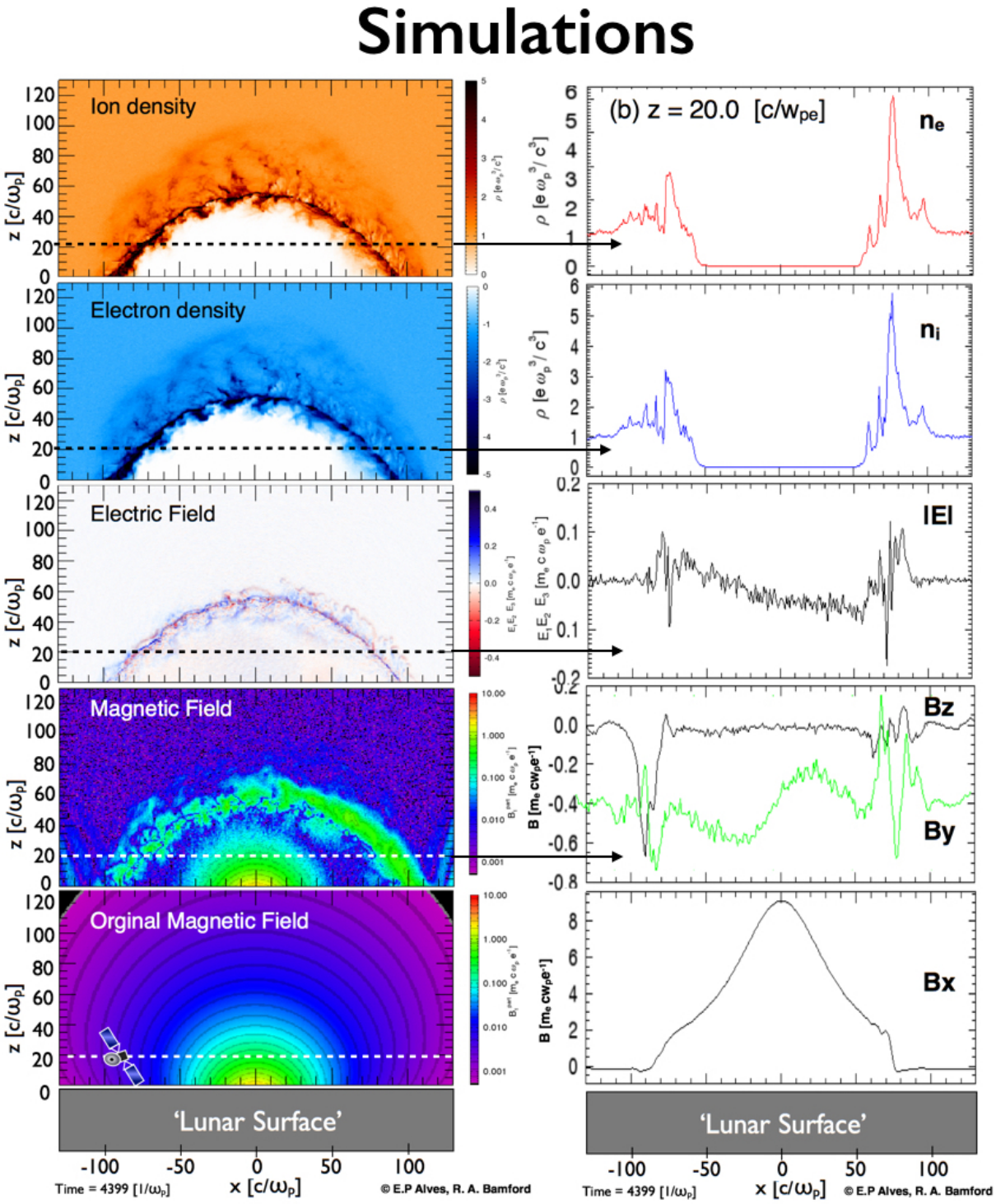

FIG. 4: (LEFT) Planar slices through the 3D simulation shown in Figure 3 showing the behaviour of the plasma densities and electromagnetic forces. The location of the plane is indicated in Figure 2. The normalised y axis represents altitude above the Moons surface. The normalised x axis represents distance along the surface of the Moon upon which a magnetic dipole field is located. (RIGHT) The simulated spacecraft diagnostic signatures of a transit through a mini-magnetosphere taken from the 3D simulation. The OSIRIS simulation is plotted so as to recreate the type of signatures that would be observed by spacecraft plasma instrumentation during a flyover of a crustal magnetic anomaly (lower most panel). A low altitude lunar spacecraft would record in a flyover transit over the surface anomaly at constant altitude of $h = 5.5 \times c/\omega_{pe}$ in normalised units the equivalent of ∼12km (for a 5cm^{-3} density plasma). The simulation is the simplest geometry with slow wind flow normal to the lunar surface, there is no drawn out magnetotail in this example. The simulated data window would be the equivalent of ∼2 to 4 minutes in duration.

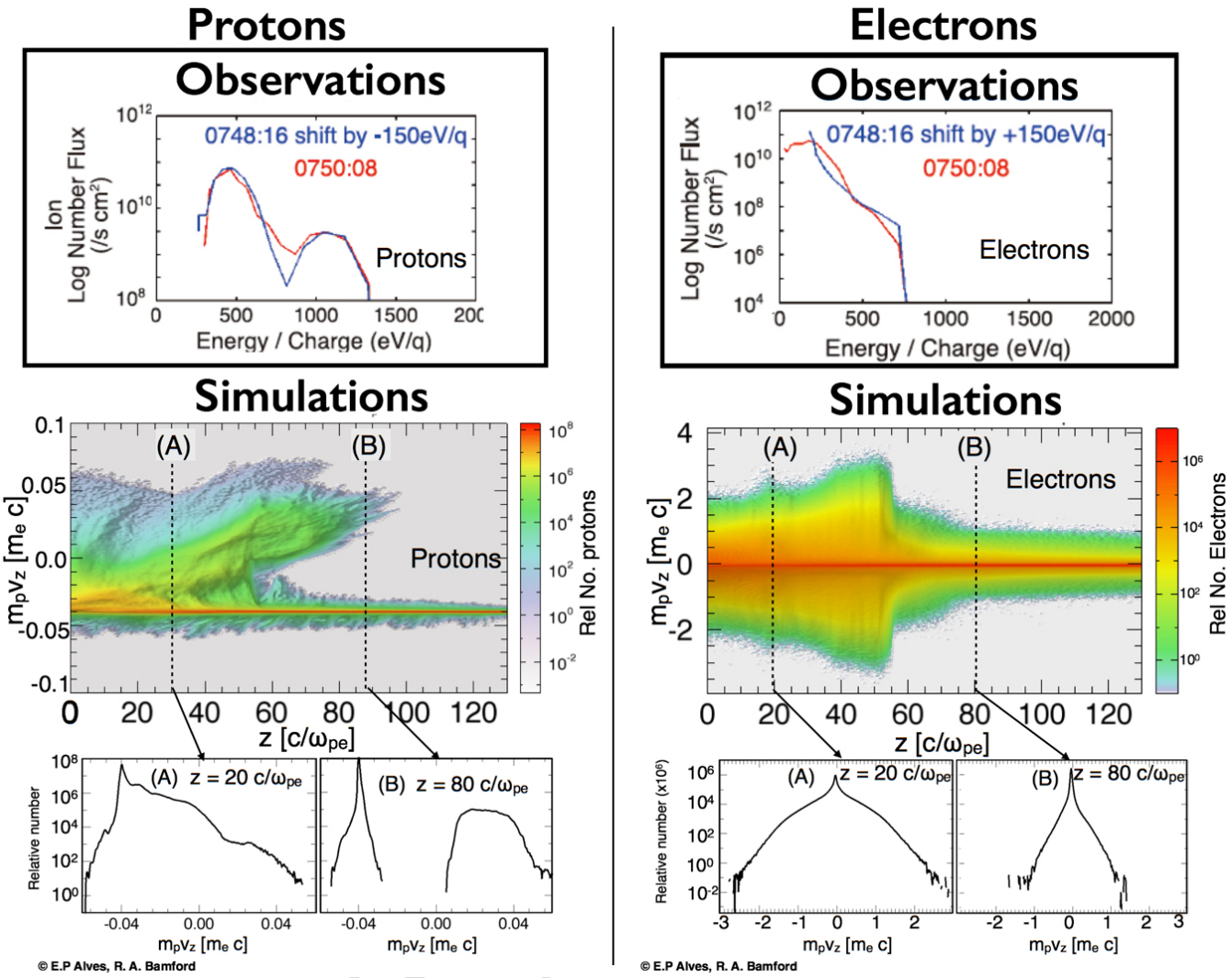

FIG. 5: (Left) Protons and (right) electron particle energy spectra comparison. (Top) Observations of the particle energy spectra observed by Kaguya spacecraft at $\sim$ 25 km altitude [44].(Middle and bottom) The vertical component of the particle momentum from the 3D simulation. Below two examples of the particle momentum distribution spectra at different altitudes from the lunar surface (A) at 20 and (B) 80 c/ω_{pe}.The latter shows the same type of reflected particle distribution seen in the observation example above (top).

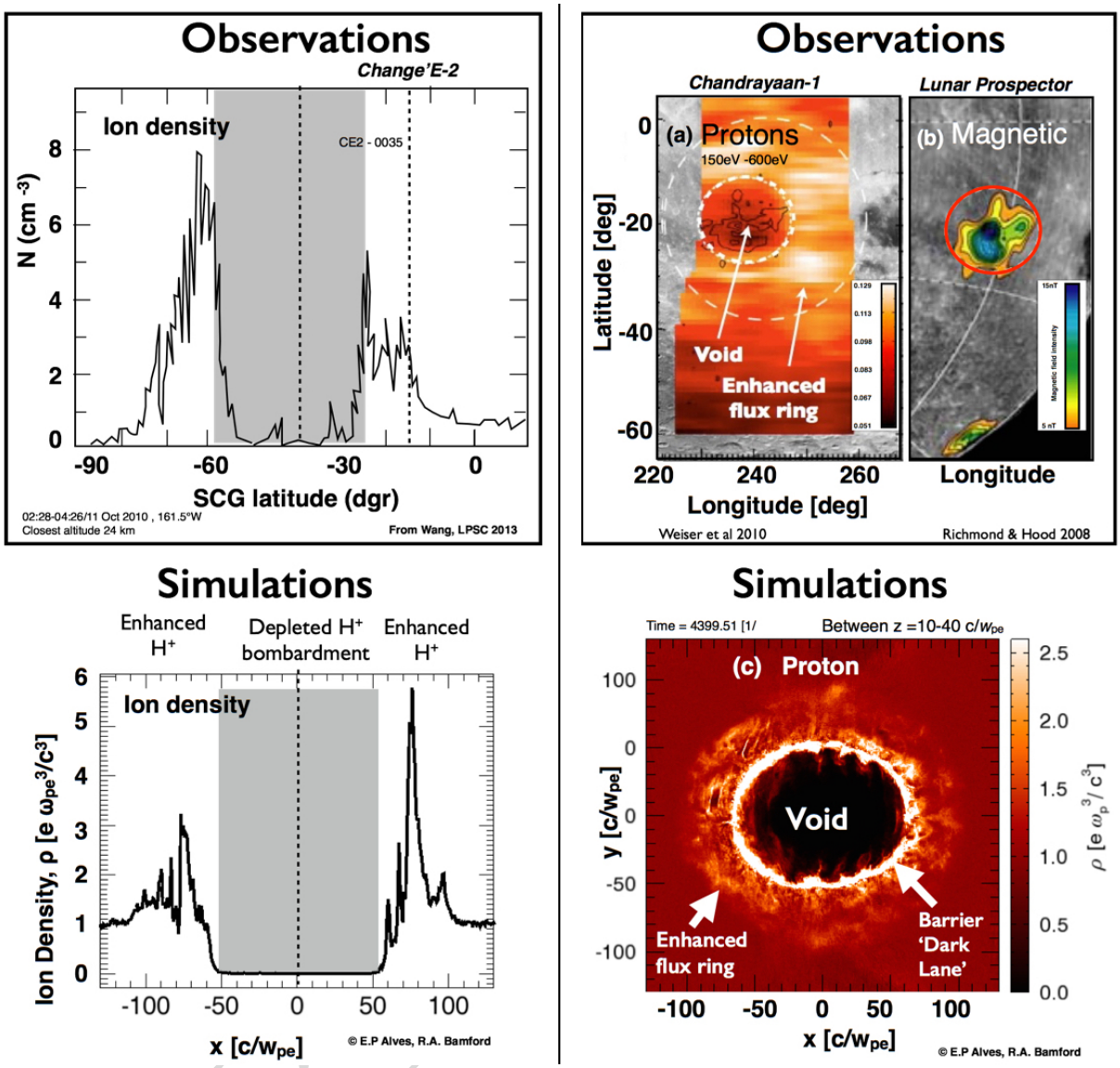

FIG. 6: A comparison of simulated and observation of proton density. (Left) Top: Proton density as a function of SCG latitude obtained from ChangeE-2 lunar orbits. region encompass the extension of the Serenitatis antipode magnetic anomaly. From Wang 2012 [38]. Bottom: The simulated relative proton deposition onto the surface of the Moon. (Right) Top: (a) Observational data from the Gerasimovich magnetic anomaly showing the spatial variation in energetic neutral hydrogen flux from the surface over the magnetic anomaly near 22°S and 240°E on the lunar farside, observed from 200 km altitude on 17 June 2009 (in unitless reflection coefficient). From [33]. (b) A map of the total magnetic field at an altitude of 30 km plotted using a Lambert equal-area projection obtained from Lunar Prospector data. From [63]. Bottom: Shows the stacked relative proton density from above from the 3D simulation (cap excluded).

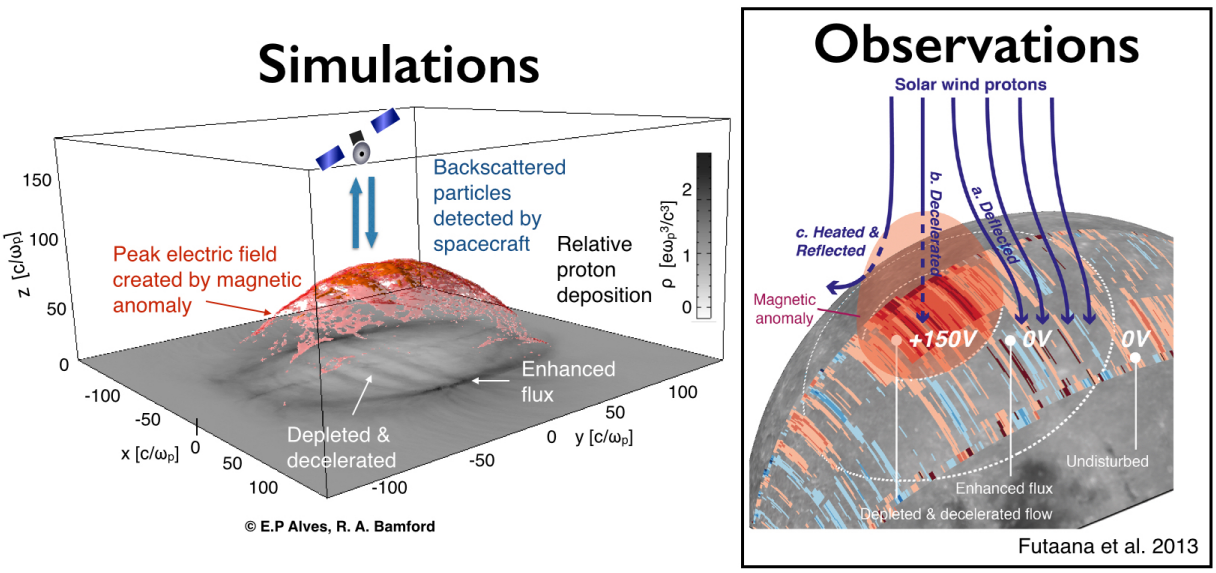

FIG. 7: A comparison between simulated and observational graphical interpretation of electric potential structure all over the isolated Gerasimovic anomaly obtained from backscattered proton flux observed by the ENA instrument on Chandryaan-1 [82].

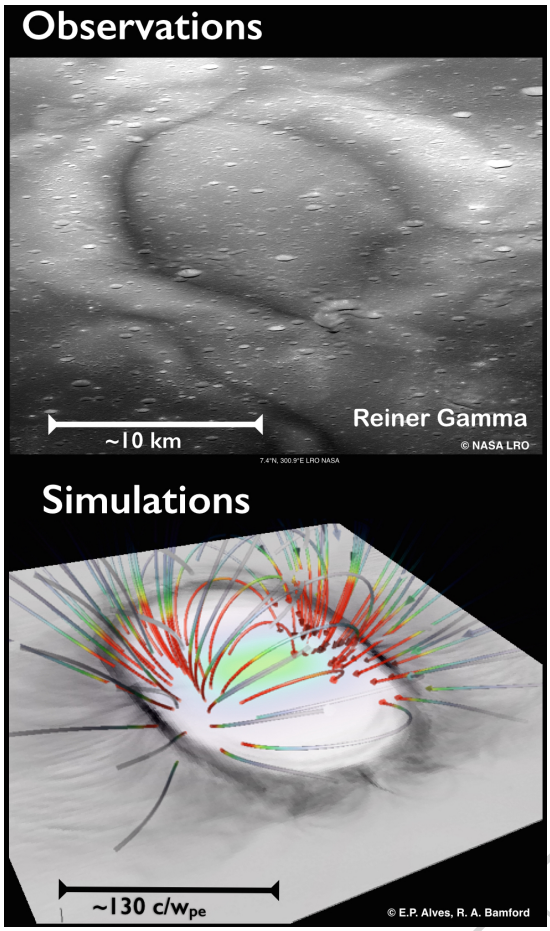

FIG. 8: Top: A image of the central region of the Reiner Gamma Formation lunar swirl taken by NASA's Lunar Reconnaissance Orbiter [84]. Bottom: A slice of the relative proton density from the 3D simulation with the initial magnetic field lines from a single subsurface dipole. The greyscale distribution shows darker for higher density of protons, whiter for less. The form and relative width of the 'dark lanes' [85] suggest the aspect ratio of dark-lane width to cavity width is similar in both cases.

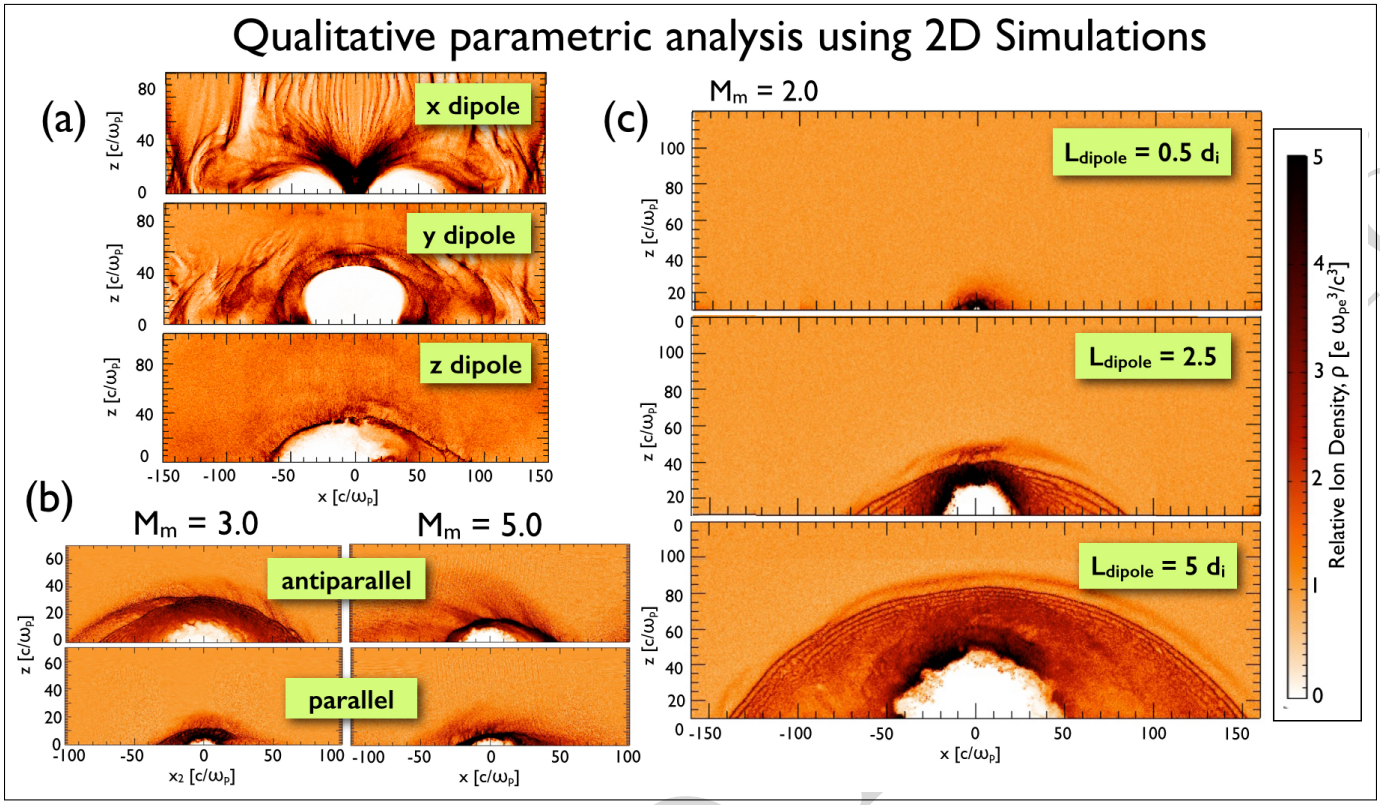

FIG. 9: A qualitative parametric analysis using 2D Simulations. (a) Different orientations of magnetic dipole axis aligned in the x,y,z direction. The vertical, x, dipole orientation (top) shows the converging particle deposition of an auroral-like structure. $M_m = 8$ and $m_p/m_e = 1836$. (b) Changes in incoming plasma flow speed and magnetic field for parallel and anti-parallel field conditions. Perpendicular shocks by cold plasma with fixed dipole size/strength ($L_{dipole} = 2$), varying magnetosonic Mach number, $M_m = 3, 5$, for parallel (bottom) and anti-parallel (top) B_{dipole}. Reduced 2D parameters: The incoming flow velocity is $\times 50$ a typical solar wind speed, proton to electron mass ratio m_p/m_e is $\sim 1/20$ realistic value, chosen for computational speed. (c) Changes to surface dipole magnitude and range. Perpendicular shocks by cold plasma with fixed magnetosonic Mach number $M_m = 2.0$ with B_{in} parallel to B_{dipole}, varying dipole size/strength $L_{dipole} = 0.5, 2.5, 5$.